

# Adaptive cancellation of mains power grid interference in continuous gravitational wave searches with a hidden markov~~Markov~~ model

Author 1, Author 2, etc. Kimpson, ~~Suvrova~~Suvorova, Liu, Melatos, Middleton, Evans, Moran, Meyers, any others?  
(Dated: October 5, 2023)

Continuous gravitational wave (GW) ~~searches are commonly~~ searches with terrestrial long-baseline interferometers are hampered by long-lived, ~~narrow peaks in the instrumental frequency spectra known as ‘lines’~~ narrowband features in the power spectral density of the detector noise, known as ~~lines~~. Candidate GW signals which ~~lie within frequency bands overlap spectrally with known lines~~ are typically vetoed. In ~~this work~~ Here we demonstrate a new line subtraction method based on adaptive noise cancellation(ANC). ANC is common, using a recursive least squares algorithm, a common approach in electrical engineering applications, including for such as processing audio and biomedical signals. We ~~show how ANC can be used in conjunction with a Viterbi search to track spin-wandering continuous wave signals near the LIGO~~ validate the line subtraction method by combining it with a hidden Markov model, a standard continuous wave search tool, to detect a synthetic continuous wave signal with an unknown and randomly wandering frequency which overlaps with the strong mains power line at 60 Hz in the Laser Interferometer Gravitational Wave Observatory. We show that the synthetic continuous wave signal can be successfully recovered once the 60 Hz line ~~has been subtracted~~. The performance of the line subtraction method with respect to the characteristics of the 60 Hz line and the parameters of the method is explored and quantified.

DOI:

## I. INTRODUCTION

Instrumental noise artifacts in gravitational wave (GW) searches with terrestrial, long-baseline interferometers are classified according to their duration and spectral properties. Short-lived, non-stationary, recurrent noise events such as optomechanical glitches typically last for seconds and exhibit distinctive spectral signatures, e.g they can be chirp-like [1–5]. Long-lived, quasi-stationary, broadband noise sources include seismic disturbances at low frequencies, test mass thermal fluctuations at intermediate frequencies, and photon shot noise at high frequencies [6–10]. Long-lived narrowband spectral artifacts ~~—~~ termed instrumental lines ~~—~~ are caused by electrical subsystems (e.g. mains power, clocks, oscillators), mechanical subsystems (e.g. test mass and beam-splitter violin modes) and calibration processes [11], although often sometimes the origin of a specific feature is unknown. Instrumental lines are disruptive, especially for continuous wave (CW) searches where the target astrophysical signal is quasi-monochromatic and resembles the noise artifact spectrally. Many above-threshold candidates discovered in ~~CW searches to date published CW searches~~ are vetoed because they coincide with known instrumental lines [12–14], for instance, in ~~CW searches involving~~ data from Observing Run 3 (O3) with the Laser Interferometer Gravitational Wave Observatory (LIGO), Virgo and the Kamioka Gravitational Wave Detector (KAGRA) [e.g. 15–17]

Several techniques have been implemented by the LIGO-Virgo-KAGRA (LVK) ~~collaboration~~Collaboration to identify, characterize and suppress instrumental noise artifacts [18, 19]. Some techniques identify and veto an

artifact (or gate ~~a segments of the data~~ data segments) based on its time-frequency signature [20–22]. Other techniques perform offline noise subtraction with reference to auxiliary data from physical environmental monitors (PEMs) [23–26]. PEMs can be used to witness correlated noise and generate a reference signal directly or elucidate and quantify multichannel couplings [27, 28]. Finally Additionally some techniques are based on machine learning [29–32]. In CW searches specifically, the distinctive amplitude and frequency (Doppler) modulations associated with the ~~Earth’s~~ Earth’s rotation and revolution respectively can be exploited to discriminate between terrestrial noise artifacts and astrophysical signals [33, 34].

In most of the situations above, the practical effect of an instrumental line is to excise the relevant part of the observing band from a CW search. That is, if an above threshold CW search candidate coincides with a known instrumental line, the candidate is vetoed under current practice without further analysis, such as comparing the expected strength of the noise line with the measured strength of the candidate<sup>1</sup>. In this paper we take a first step towards lifting the above limitation. We introduce an adaptive noise cancellation (ANC) scheme based on an adaptive recursive least squares (ARLS) method which suppresses narrowband noise proportional to a known PEM reference signal. We then apply the ANC scheme to a CW search algorithm based on a hidden Markov model (HMM) which detects and

<sup>1</sup> A regularly updated log of narrowband instrumental lines in the LVK detector is maintained at [dcc.ligo.org/LIGO-T2100200/public](http://dcc.ligo.org/LIGO-T2100200/public) for public reference.

tracks quasi-monochromatic GW signals with wandering frequency and has been tested and validated thoroughly in multiple LVK searches [12–14, 35]. We demonstrate with synthetic data that the ANC scheme and HMM algorithm together can successfully detect a GW signal lying under the ~~60Hz~~-~~60 Hz~~ mains power line, if the signal exceeds a well-defined minimum amplitude. The approach extends naturally to other instrumental lines, a topic for future work.

The paper is organized as follows. In Section II we outline ~~our~~ a mathematical model for the ~~60Hz~~ mains power spectral ~~60 Hz~~ mains power line and the PEM reference signal, and justify the assumptions of the model by reference to ~~the strain and environmental~~ data from the LIGO Livingston interferometer. In Section III we introduce ANC formulated as an ARLS method. ~~We go on in Section IV to deploy the ANC method. In Section IV we validate the ANC scheme on synthetic GW strain data, in conjunction with an HMM Viterbi solver applied to synthetic GW strain data algorithm, and demonstrate the successful recovery of a monochromatic GW signal frequency-wandering CW signal. In Section V we quantify the performance of the HMM Viterbi algorithm and ANC scheme as a function of the key parameters of the mains power interference and ANC filter. Concluding remarks are given in Section VI.~~

## II. POWER GRID INTERFERENCE

The goal of this paper is to detect a ~~quasi-normal~~ ~~quasi-monochromatic~~ GW signal in a data stream contaminated by two kinds of noise: additive Gaussian noise which is fundamental and irreducible, and additive non-Gaussian interference from a long-lived narrow spectral feature which can be filtered out in principle given an accurately measured reference signal. For this work we consider the spectral line at 60 Hz that results from the North American alternating current power grid as the additive non-Gaussian interference, ~~as it is a long-standing impediment to many CW searches with the LIGO interferometers~~. In Section II A we briefly review the 60 Hz LIGO interference line before proceeding in Section II B to specify the assumed mathematical forms of the interference and reference signals. In Section II C we justify the assumptions of Section II B by analysing differential arm length (DARM channel) and environmental (power grid monitoring) data from the LIGO interferometers.

### A. LIGO 60 Hz Interference

LIGO data contains multiple long-duration narrow lines (~~e.g.~~ Fig. 1) in addition to the usual Gaussian noise. ~~These lines are shown in Figure 1 where we plot the amplitude spectral density of the GW strain channel~~

~~\*:DCS-CALIB\_STRAIN\_C01\_AR for both LIGO-Hanford (H1, orange curve) and LIGO-Livingston (L1, blue curve). The small amplitude random fluctuations are the result of Gaussian noise whereas the large amplitude spikes are the long-duration lines. The provision of mains power electricity in North America via an alternating current with frequency 60 Hz leads to a line in the LIGO data at the corresponding frequency. The coupling between the mains power and the gravitational wave data channel can occur since power spectral density of the LIGO noise. The mains power couples to the GW strain channel, because the performance of the high-sensitivity electronic components within LIGO varies with respect to the input power voltage. Additionally, the magnetic fields that arise from the AC mains supply can couple with the magnets on the LIGO couple to magnets on optical components. Whilst some~~

~~Some~~ spectral lines are static, ~~the 60Hz~~ but the 60 Hz line wanders in time, due to variations in the load in the North America power grid at any one time (e.g. Fig. 2). This time variation can further impact the detector sensitivity over a broader frequency band. American power grid. The wandering is displayed in the cascade plot in Figure 2, where the amplitude spectral density of the output signal of the LIGO-Hanford PEM channel H1:PEM-CS\_MAINSMON\_EBAY\_1\_DQ is plotted for 210 5-min samples stacked vertically. The peak of the amplitude spectral density varies from 59.969 Hz to 60.053 Hz, across the 210 samples with an average value of 60.004 Hz. Its full width half maximum varies from 5.294 mHz to 29.377 mHz, with an average value of 10.749 mHz. For a full review of LIGO spectral artifacts, including the 60 Hz line, we refer the reader to [11].

~~The 60 Hz line occurs in the neighbourhood of plausible astrophysical signals. For example, mass quadrupole radiation from a rotating mountain on the Crab pulsar would be emitted at twice the star's spin frequency, viz. 30.2 Hz [13, 14].~~

### B. Statement of the problem: signal and noise models

Let  $x(t)$  denote the scalar time series output by the ~~“science”~~ or ~~GW~~ strain channel of a LIGO-like long baseline interferometer. Suppose that  $x(t)$  is sampled at discrete times  $t_n$ , with  $1 \leq n \leq N$  and uniform sampling interval  $\Delta t = t_n - t_{n-1}$ . Let  $r(t)$  denote the scalar time series output by the environmental ~~reference~~ channel relevant for filtering interference; here  $r(t)$  is of one of the three phases of mains power measured at some reference point in the detector. The reference signal is usually sampled less frequently than  $x(t)$  at discrete times  $t_{n_k}$ , with  $1 \leq k \leq K$  and  $1 \leq n_k \leq N$ . We assume for the sake of convenience that every  $t_{n_k}$  coincides with some  $t_n$  for all  $k$ , but the condition is not essential.

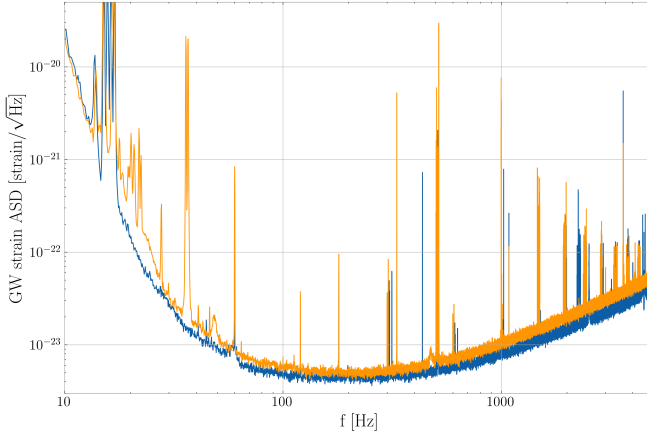


FIG. 1. Sensitivity plot for LIGO-Hanford (orange) and LIGO-Livingston (blue) for a snapshot of data ( $\sim 10$ – $10.0$  minutes) from O3 (channel \*:DCS-CALIB\_STRAIN\_C01\_AR, see Ref. [36, 37]). The vertical axis plots the amplitude spectral density of the detector noise in units of  $\text{Hz}^{-1/2}$ , while the horizontal axis plots the observation frequency in units of Hz. The spectral line at 60 Hz is clearly visible as a spike rising three decades, along with multiple other instrumental lines at other frequencies.

The strain channel is composed of a gravitational wave signal  $h(t)$ , non-Gaussian-non-Gaussian interference  $c(t)$  (sometimes called “clutter”) and Gaussian noise  $n(t)$  in a linear combination:

$$x(t) = h(t) + c(t) + n(t) . \quad (1)$$

In this paper the gravitational wave signal takes the form predicted by Jaranowski *et al.* [38] for a biaxial rotor, e.g. a neutron star (NS) emitting continuous gravitational waves at multiples of the star’s spin frequency  $f_*$ . The GW signal is quasimonochromatic/quasi-monochromatic, amplitude-modulated by the rotation of the Earth and frequency-modulated-frequency-modulated by the Earth’s orbital motion. The noise  $n(t)$  is white with  $\langle n(t_n)n(t_{n'}) \rangle = \sigma_n^2 \delta_{nn'}$ . Noise samples  $n(t_n)$  are drawn from a Gaussian distribution with zero mean and variance  $\sigma_n^2$ . The interference clutter  $c(t)$  takes a form determined by instrumental processes but is generally a long-lived narrow, narrowband spectral feature. We can relate  $c(t)$  to the instrumental mains voltage  $r(t)$  in the following this paper.

Mains power is characterized by three properties. First, the frequency is maintained at a constant value across the grid to ~~to~~ a good approximation by internal grid mechanisms (effectively a phase locked loop), with central frequency  $f_{\text{ac}} = 60$  Hz in North America. A slow periodic modulation occurs around  $f_{\text{ac}}$  with a small amplitude  $\Delta f_{\text{ac}} \lesssim 0.5$  Hz and period  $P$ , which wanders randomly and uniformly in the range  $0 \leq P \leq P_{\text{max}}$ . ~~Secondly~~ Second, the phase offset  $\Theta(t)$  of the voltage  $r(t)$

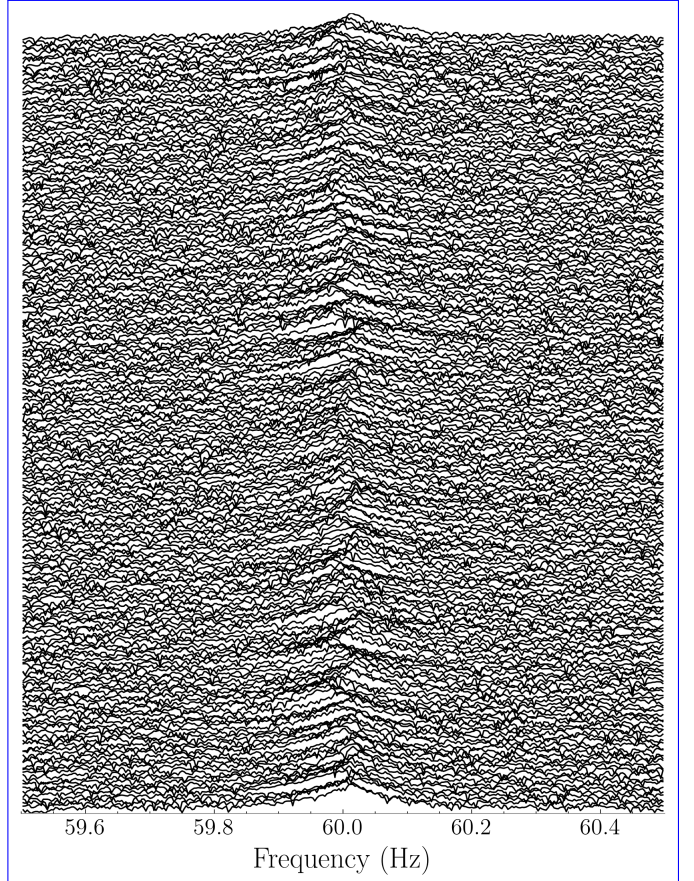


FIG. 2. Cascade plot showing the temporal evolution of the amplitude spectral density (units:  $\text{Hz}^{-1/2}$ ) of the Hanford-LIGO-Hanford mains-power PEM monitor H1:PEM-CS\_MAINSMON\_EBAY\_1\_DQ (corner station, phase 1) over time as a function of frequency (units: Hz). Each trace corresponds to 320s ( $\approx 5$  min) of data (210 lines plotted traces stacked vertically). The wandering peak of the 60Hz instrumental mains power 60Hz line wanders by  $\approx \pm 30$  mHz about its central value can be seen time-averaged frequency.

wanders stochastically. We assume that the phase noise is white and Gaussian, with  $n_\Theta(t_n)$  drawn from a Gaussian distribution with zero mean and variance  $\sigma_\Theta^2$ , and i.e.  $\langle n_\Theta(t_n)n_\Theta(t_{n'}) \rangle = \sigma_\Theta^2 \delta_{nn'}$ . Third, the voltage amplitude,  $A_r(t)$ , is random. We assume that samples  $A_r(t)$  are distributed uniformly within  $[A_{\text{ac}} - \Delta A_{\text{ac}}, A_{\text{ac}} + \Delta A_{\text{ac}}]$ . We can then write the reference voltage as,

$$r(t) = A_r(t_n) \cos [2\pi f_{\text{ac}} t + \Theta(t)] + n_r(t_n) , \quad (2)$$

with

$$\Theta(t) = 2\pi\Delta f_{\text{ac}} \cos \left[ \frac{2\pi t}{P(t_n)} \right] + n_\Theta(t_n) , \quad (3)$$

for  $t_n \leq t \leq t_{n+1}$ . That is, at time  $t_n$ , random variables  $A_r(t_n)$ ,  $A_c(t_n)$ ,  $P(t_n)$  and  $n_\Theta(t_n)$  are drawn from the distribution  $\mathcal{U}[A_{\text{ac}} - \Delta A_{\text{ac}}, A_{\text{ac}} + \Delta A_{\text{ac}}]$ ,  $\mathcal{U}[0, P_{\text{max}}]$ , and

$\mathcal{N}[0, \sigma_0^2]$  respectively. Equation (2) then runs forward over an interval of length steps forward over a time interval  $\Delta t$ . Hence, that is,  $r(t)$  is discontinuous at each sampling time from one time step to the next due to random sampling. In Equation (2),  $n_r(t_n)$  is the reference signal measurement noise at  $t_n$ , assumed to be white and Gaussian with  $r_r(t_n) n_r(t_n)$  drawn from a Gaussian with zero mean and variance  $\sigma_r^2$ . All the white measurement and process noises are assumed to be independent.

Mains power couples into the strain channel in various complicated ways, e.g. through electronic devices, or inductively through ambient magnetic fields. A central assumption in this work is that the interference in the strain channel is an exact, amplitude-scaled replica of the reference signal up to a delay  $\tau_{\text{delay}}$  which is attributed to spatial propagation effects between the reference measurement front and the interferometer mirrors or dark front between the PEM site and the GW-sensing apparatus. Hence we can express the interference clutter as,

$$c(t) = A_c(t'_n) \cos [2\pi f_{\text{ac}} t' + \Theta(t')] ,$$

as,

$$\begin{aligned} c(t) &= A_c(t_n - \tau_{\text{delay}}) \cos \left[ 2\pi f_{\text{ac}}(t_n - \tau_{\text{delay}}) \right. \\ &\quad \left. + \Theta(t_n - \tau_{\text{delay}}) \right] , \end{aligned} \quad (4)$$

for  $t_n \leq t \leq t_{n+1}$  and  $t' = t_n - \tau_{\text{delay}}$ . The amplitude  $A_c$  is distributed as  $\mathcal{U}[A_{\text{ac}}, A_{\text{ac}} + \Delta A_{\text{ac}}] \mathcal{U}[A_{\text{ac}} - \Delta A_{\text{ac}}, A_{\text{ac}} + \Delta A_{\text{ac}}]$ . For this work we consider  $0 \leq \tau_{\text{delay}} \leq 10\Delta t$ , but wider or narrower ranges are possible and straightforward to be implemented. The assumptions of an exact replica between the interference and the reference implement. The assumption that  $c(t)$  is a scaled replica of  $r(t)$  is tested in the following section.<sup>2</sup> Section II C.

### C. Cross-correlating the interference Coherence between $x(t)$ and reference $r(t)$

A key assumption of the construction in Section II B is that the 60 Hz noise that is interference recorded in the reference PEM channel is also present in the LIGO strain channel. That is, the noise recorded in the PEM channel mains voltage recorded by the PEM is imprinted onto the strain channel up to a proportionality constant and time delay. In order to test this assumption we

<sup>2</sup> TK: Why are the amplitudes of  $A_r$  and  $A_c$  distributed differently?

cross-correlate the calculate the coherence between the strain channel and the PEM channel. If there is a noise signal at 60 Hz present in both channels then it should be revealed by this cross-correlation. We use open sourced

The coherence between two time series  $x(t)$  and  $r(t)$  is given by

$$C_{xr}(f) = \frac{|P_{xr}(f)|^2}{P_{xx}(f)P_{rr}(f)} \quad (5)$$

where  $f$  is the frequency,  $P_{xx}$  is the (cross) power spectral density and  $0 \leq C_{xr}(f) \leq 1$ .  $C_{xr}(f) = 0$  indicates that the two signals are completely unrelated, whilst  $C_{xr}(f) = 1$  indicates that the two signals have an ideal, noiseless, linear relationship i.e.  $x(t) = g(t) * r(t)$  for impulse response function  $g(t)$ . If  $0 < C_{xr}(f) < 1$  then this indicates that the relationship between  $x(t)$  and  $r(t)$  is non-linear, either due to measurement noise or else contributions to  $x(t)$  from additional signals. Heuristically, for linear systems,  $C_{xr}(f)$  can be understood as the fraction of the power in  $x(t)$  that is produced by  $r(t)$ , at  $f$ .

We use data for the strain and PEM channels from the first part of the third LIGO observing run, O3a [36]. This data is These data are obtained via the Gravitational Wave Open Science Center LIGO Data Grid<sup>2</sup> using the GWPY package [39]. In the auxiliary O3a data there are 9 there are nine independent PEM channels at both LIGO-Livingston and 7 PEM channels at LIGO-Hanford that directly measure the mains voltage<sup>3</sup>. For this work In this paper we consider just the LIGO-Livingston data. as they suffice to make the point. Specifically, there are 3 PEM mains voltage monitors in the electronics bay in each of the X-arm end station (EX), the Y-arm end station (EY) and the corner station (CS). Each of the three PEMs at each station measures a separate component of three-phase mains power. The strain data is obtained at a rate of are sampled at 16384 Hz and downsampled to 4096–1024 Hz to match the sampling rate of the PEM channels. In Figure ?? we show the coherence between each of the 9 PEM channels and the

Figure 3 displays  $C_{xr}(f)$  between the high latency, calibrated strain channel L1:DCS-CALIB\_STRAIN\_C01\_AR and each of the nine reference PEM channels over a 10 minute time period interval. For all channels there is a clear coherence feature at 60Hz. The coherence

<sup>2</sup> <https://computing.docs.ligo.org/guide/computing-centres/ldg/>

<sup>3</sup> <https://git.ligo.org/detchar/ligo-channel-lists/-/blob/master/03/L1-03-pem.ini>

feature is typically large, with values  $> 0.5$  for 7 of the 9 PEM channels. Compared to the other channels, the coherence is particularly weak for the channels `L1:PEM-EY_MIC_VEA_PLUSY_DQ` spike in the  $C_{xy}(f)$  at 60 Hz, with a mean amplitude = 0.85 (unitless).

It is important to note that whilst  $C_{xy}(f = 60\text{Hz})$  between  $x(t)$  and `L1:PEM-CS_MIC_LVEA_INPUTOPTICS_DQ`. These channels corresponds to microphone PEMs in the LIGO vacuum equipment area and so would be less sensitive to the 60Hz noise than e.g. `L1:PEM-EY MAINSMON EBAY_1.DQ` which directly measures the voltage. In Figure 4 we also show  $r(t)$  is strong, it is also time variable. Figure 4 displays the coherence spectrogram, i.e. the time-varying coherence, between the strain channel and the PEM channel `L1:PEM-CS_MAINSMON_EBAY_1.DQ`. The coherence is calculated across (c.f. top panel, Figure 3) over a 1 hour time interval (c.f. the 10 s windows of data. That is, each column of the spectrogram has a width of minute interval of Figure 3).  $C_{xy}(f)$  is calculated in 10-s blocks; that is, every pixel in Figure 4 is 10 s. We again observe similar results to Figure ?? where wide horizontally. We use a Fourier transform window of length 0.5 s, with each window overlapping by 0.25 s (c.f. Welch's method, [40]). Similar results are observed to Figure 3; there is a clear, strong coherence (mean value = 0.73) spectral feature at 60Hz. Additional coherence features can also be seen at at  $\sim 200$  Hz and  $300$  Hz 60 Hz which persists across the full 1 hour time interval. However, whilst the feature is persistent,  $C_{xy}(f = 60\text{Hz})$  is not constant across the entire interval. Instead it changes in time, with a variance = 0.018. These variations are evident in the changing colours of the spectrogram at 60 Hz, leading to an apparent “patchiness” of the line. Additional features in the  $C_{xy}(f)$  spectrum are seen near 0.2 kHz and 0.3 kHz, corresponding to different frequency noise instrumental lines recorded by the PEM that also which imprint onto the strain channel and are unrelated to the mains power. Similar results are obtained for the other PEM channels shown in Figure 3. Figures 3 and 4 justify in part the assumptions in Section II B. These results showing a strong coherence between the strain and PEM channels demonstrate that our assumptions of Seetion II B are justified.

### III. ADAPTIVE NOISE CANCELLATION ANC SCHEME

Adaptive Noise Cancellation noise cancellation (ANC) is a method for recovering an estimate of an underlying signal which has been corrupted or obscured by some additive noise interference [41]. In contrast to other common optimal filtering methods (e.g. Wiener, Kalman) ANC requires no *a-priori-a priori* knowledge of either the signal or the noise. Instead, ANC makes use of a reference input which is correlated in some

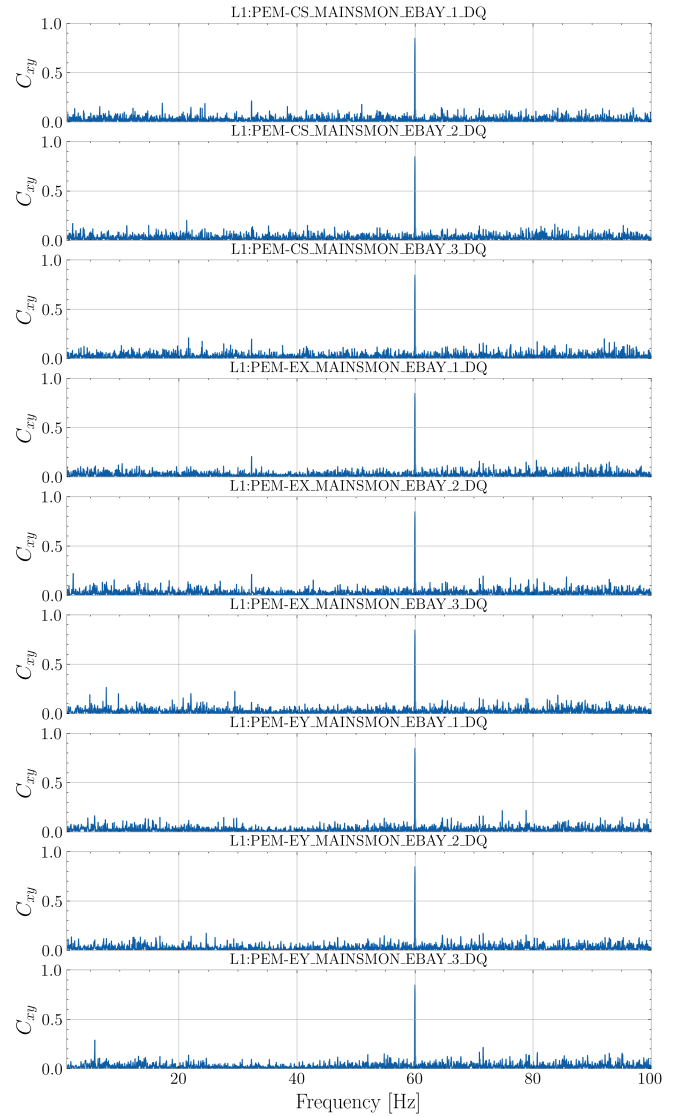


FIG. 3. Coherence  $C_{xy}$ , defined by Equation (5), between the LIGO-Livingston strain channel `L1:DCS-CALIB_STRAIN_C01.AR` and the 9-nine mains-power PEM channels over during a 10 minute observation periodinterval. Clear features at 60 Hz are present in all of the channels. The coherence is weakest for these PEM channels which do not measure voltage directlyevery channel, but instead are microphones in the LIGO vacuum equipment area with amplitudes  $> 0.8$  (unitless).

unknown way to with the noise in the primary signal. This reference can then be The reference is filtered and subtracted from the primary data series so as to recover the underlying signal. For our purposes, the primary timeseries is the gravitational-wave strain channel,  $x(t)$ (Equation (1)) Equation (1), and the reference is a PEM recording voltage data from the power grid a mains voltage,  $r(t)$ (Equation (2)), Equation (2). The objective of ANC is then to remove the clutter  $c(t)$  off in

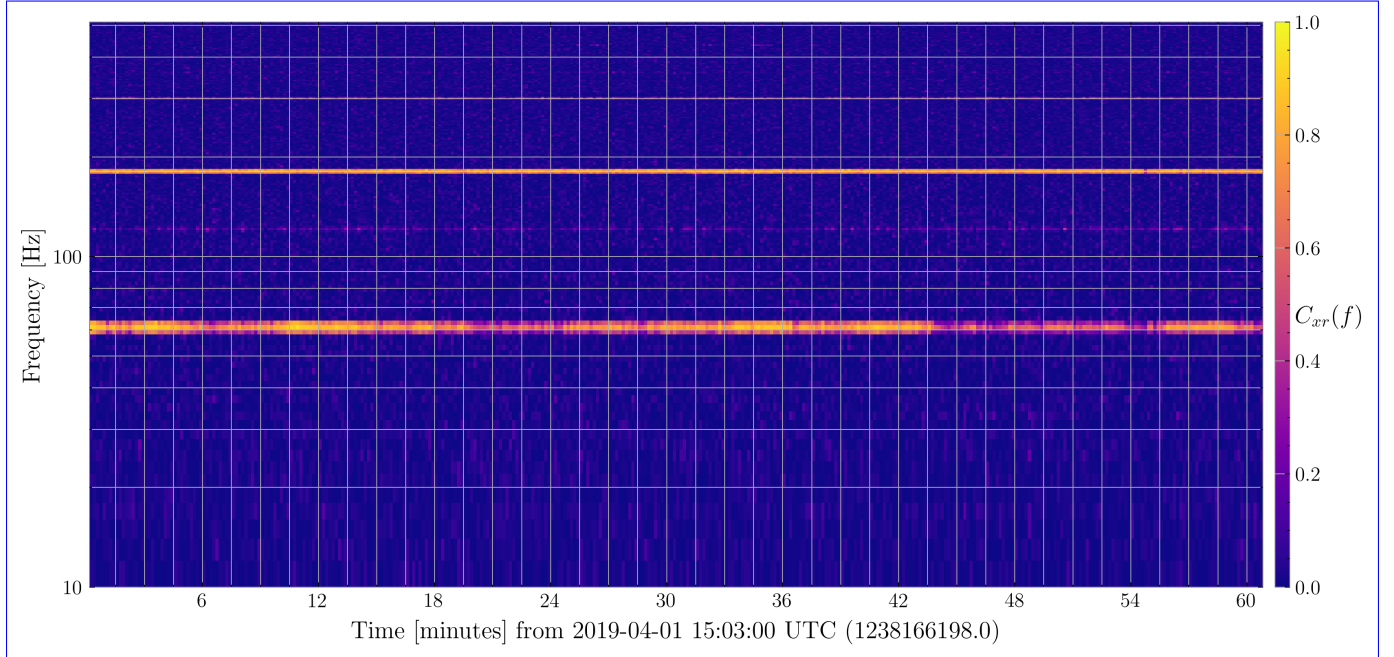


FIG. 4. Coherence spectrogram between the strain channel L1:DCS-CALIB\_STRAIN\_C01\_AR and the PEM channel L1:PEM-CS\_MAINSMON\_EBAY\_1\_DQ covering a 10-minute-1 hour period of O3 data. The x-axis is the time in minutes from the start of O3a, separated into 10s bins. The y-axis is the frequency in Hz. The pixel colour denotes the coherence  $C_{xy}$ , Equation (5), in that time-frequency bin. A strong coherence is observed at 60 Hz–60 Hz due to the main power interference. Additional coherence features can also be observed at ~200 Hz–0.2 kHz and 300 Hz–0.3 kHz due to instrumental lines of a different provenance c.f. Fig. Figure 1.

Equation (1) with the aid of  $r(t)$  whilst leaving  $h(t)$  i.e. the signal of interest, intact. We now describe the ANC implementation used in this work.

The reference  $r(t)$  is used to construct

### A. Filter

The first step in implementing ANC is to convert  $r(t)$  into an estimate of the clutter,  $\hat{c}(t)$ . The clutter estimate can then be subtracted from the primary signal in the time domain, defining a residual  $e(t)$ :

$$e(t) = x(t) - \hat{c}(t) . \quad (6)$$

As In the limit  $\hat{c}(t) \rightarrow c(t)$ , one obtains  $e(t) \rightarrow h(t) + n(t)$  and we recover recovers a noise cancelled timeseries. The clutter estimate is modelled by a finite duration impulse response (FIR) filter:

$$\hat{c}_k = \mathbf{w}^\top \mathbf{u}_k . \quad (7)$$

where  $\hat{c}_k$  In Equation (7),  $\hat{c}_k = \hat{c}(t_{n_k})$  is the clutter estimate at a discrete timestep  $k$  (i.e.  $\hat{c}_k = \hat{c}(t_{n_k})$ ) the  $n_k$ -th time step,  $\mathbf{u}_k$  is the tap-input vector composed of  $M$  running samples of the reference signal arranged backwards in time:

$$\mathbf{u}_k = [r_k, r_{k-1}, \dots, r_{k-M+1}] , \quad (8)$$

and  $\mathbf{w}$  is the tap-weight vector:

$$\mathbf{w} = [w_1, w_2, \dots, w_M] . \quad (9)$$

We want

The goal of ANC is to determine the optimal tap weights  $\mathbf{w}_{\text{opt}}$ , those which that minimise the mean square error cost function:

$$\mathbf{w}_{\text{opt}} = \arg \min \sum_{t=t_1}^{t=t_N} \sum_{k=1}^K \lambda^{K-k-1} |e(t)_k|^2 , \quad (10)$$

This minimization problem where  $0 \leq \lambda \leq 1$  is a “forgetting factor” which gives exponentially less weight to older samples and can be freely chosen. The choice of  $\lambda$  in this paper is discussed in Section III B. The minimization problem described by Equation (10) can be solved by way of an adaptive recursive least squares (ARLS) method which we now describe in many ways. Here we implement an ARLS algorithm. The algorithm is outlined in Section III B

### B. Adaptive Recursive Least Squares Method ARLS algorithm

We now outline the ARLS method to compute the optimal tap weights and estimate the noise-subtracted signal.

As its name implies, the ARLS algorithm is adaptive, in the sense that the weights  $\mathbf{w}$  are continually updated based on new data. It is also recursive, in the sense that  $\mathbf{w}$  are updated iteratively as new data arrives, rather than reprocessing all previous data. Abbreviated pseudocode is presented below for the sake of reproducibility and the reader's convenience. The reader is referred to standard signal processing textbooks, e.g. [42] for more information.

ARLS proceeds as follows:

1. Initialise the tap weights  $\mathbf{w} = \mathbf{0}$  and a covariance matrix  $\mathbf{P} = \delta^{-1}\mathbf{I}$ ,  $\mathbf{P} = \langle \mathbf{w}\mathbf{w}^T \rangle = \delta^{-1}\mathbf{I}$  of rank  $M$  for regularisation parameter  $0 < \delta \ll 1$  and an  $M \times M$  identity matrix  $\mathbf{I}$  of rank  $M$  where the superscript  $T$  symbolises transposition.

2. For  $k = 1, \dots, K$ :

$$1 \leq k \leq K:$$

- (a) Estimate the clutter  $\hat{c}_k$  by Equation 7 from Equation (7)
- (b) Calculate the residual  $e_k$  by Equation 6 from Equation (6)
- (c) Calculate the gain vector

$$\mathbf{g}_k = \frac{\mathbf{P}\mathbf{u}_k}{\lambda + \mathbf{u}_k^T \mathbf{P} \mathbf{u}_k} \quad (11)$$

- (d) Update the tap weights

$$\mathbf{w}_{\pm k} = \mathbf{w}_{k-1} + e_k \mathbf{g}_k \quad (12)$$

- (e) Update the covariance matrix

$$\mathbf{P}_{\pm k} = \mathbf{P}_{k-1} \lambda^{-1} \mathbf{P} - \mathbf{g}_k \lambda^{-1} \mathbf{P}_k \mathbf{u}_k^T \lambda^{-1} \mathbf{P}_{k-1} \quad (13)$$

The algorithm pseudocode is also illustrated in Figure 5 via a block diagram. At time  $t$  the filter receives the reference signal  $r(t)$  and produces an estimate of the clutter  $\hat{c}(t)$ , given the current tap weights  $\mathbf{w}$ . By comparing  $\hat{c}(t)$  with the strain data  $x(t)$  a residual is calculated  $e(t)$ . The residual is then used in conjunction with  $r(t)$  to update the weights and the algorithm continues iteratively.

ARLS has two free parameters: the order parameter  $M$  and the “forgetting factor”, the forgetting factor  $\lambda$ , which is chosen so as to give exponentially less weight to older samples. The choice and the regularisation parameter  $\delta$ . Larger values of  $M$  influences the latency of the FIR filter, corresponds to an increased model complexity. Whilst this generally increases the accuracy of the resulting estimates, it also increases the computational overhead and the filter accuracy hence the latency between receiving the input

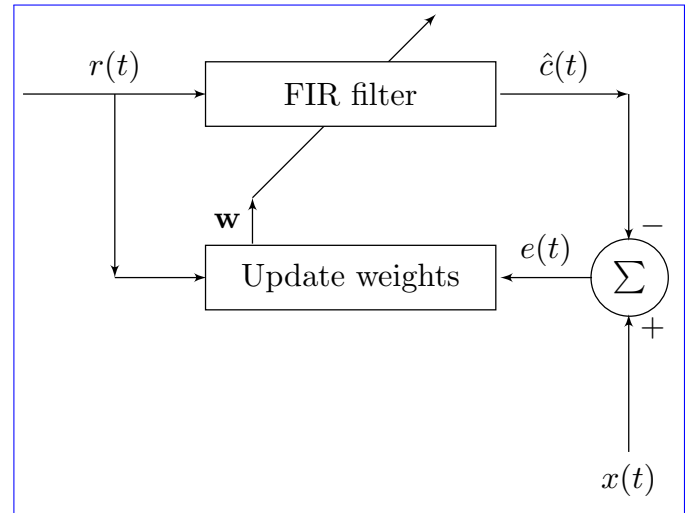


FIG. 5. Block diagram of the adaptive recursive least squares (ARLS) method described in Section III B. The reference signal  $r(t)$  is passed to an FIR filter to construct an estimate of the clutter  $\hat{c}(t)$ . Subtracting the clutter estimate  $\hat{c}(t)$  from the primary signal  $x(t)$  provides a residual  $e(t)$  which can then be used to update the weights  $\mathbf{w}$  of the FIR filter. The method proceeds iteratively. The diagonal line across the FIR filter block denotes that the parameters of the block (i.e.  $\mathbf{w}$ ) are being updated, but are not part of the signal processed by the block.

data and updating the weights. In Sec. IV we trial a selection of  $M$  values for synthetic GW data. The forgetting factor  $\lambda$  ranges between 0 and 1, with  $\lambda = 1$  corresponding to infinite memory, causing the filter becomes an ordinary least squares method a “growing window” RLS [43, 44]. In this work we use  $\lambda = 0.9999$ . Different values of  $\lambda$  are investigated in Section V B. The regularisation parameter  $\delta$  must be “suitably chosen” [45, 46]. A large  $\delta$  leads to rapid convergence of the ARLS algorithm, but with correspondingly larger variance in the parameter estimates before convergence. Conversely, a smaller  $\delta$  leads to slower convergence and smaller variance in the parameter estimates. General guidelines for choosing  $\delta$  are not readily available. Instead  $\delta$  is typically empirically selected for the particular problem. In this work we found  $\delta = 100$  to be a reasonable choice, since we have a large uncertainty in our initial estimate of the weights. We refer the reader to Chapter 9 of Ref. [42] for a full review of adaptive least squares estimation in the context of linear filtering.

#### IV. HMM VALIDATION TESTS WITH AN HMM

We want to test the ANC method described in the preceding section by trying scheme in Section III by

combining it with a HMM to search for a continuous wave signal which has an initial frequency  $f_{\text{GW}}(t=0) = 60\text{Hz}$ , coincident with the instrumental line from the mains power grid. We search for the CW signal using a HMM scheme based on the Viterbi algorithm [47, 48]. Specifically, we use the method CW signal with randomly wandering frequency, which overlaps the mains power line. Many other validation tests are possible, of course, and no individual test represents the final word on the efficacy of the scheme. Nonetheless, HMM-based searches are a key element of the data analysis program of the LVK Collaboration generating a substantial corpus of published results [49–54]. In the context of this paper, validations tests involving a HMM are especially powerful, because they present the ANC scheme with an additional challenge: to subtract the mains power line well enough to reveal an underlying CW signal, which is itself “noisy” (in the sense that its frequency wanders) rather than monochromatic. That is, the ANC-HMM combination is tasked to not only remove the stochastic 60-Hz interference but also distinguish it from the process noise in the CW signal’s frequency. If the ANC succeeds in this complicated task, one may be confident that it also succeeds in the easier task of subtracting the mains power line to reveal an underlying CW signal whose frequency is constant.

In what follows, we employ the HMM scheme introduced by Suvorova *et al.* [35], which has been thoroughly tested through multiple LVK searches [12–14]. We do not cover any details of the HMM scheme in this work and refer the reader to Suvorova *et al.* [35] for further information. The GW signal is obscured in the data by the presence of the mains power instrumental line. A synthetic CW signal  $h(t)$ , whose frequency executes an unbiased random walk, is injected into synthetic Gaussian noise  $n(t)$  typical of the LIGO detectors. A simulated 60-Hz mains power line  $c(t)$  is superposed, whose properties mimic the real system (see Section II A). The challenge is to try to recover the signal by first recover the  $h(t)$  by passing the data  $x(t)$  through the ANC filter before using the HMM tracker on this filtered dataset to try to recover the signal and feeding the output into the HMM tracker. In Section IV A we describe how we create a synthetic dataset time series  $x(t)$ . In Section IV B we introduce present a representative example, illustrating the frequency tracking and compare the HMM’s ability to detect and track  $h(t)$  before and after ANC. In Section V A we explore the performance of the ANC filter in response to different characteristics of the interference signal, e.g. variations in the central frequency  $f_{\text{ac}}$  relative to the initial GW frequency. In Section V B we investigate the performance of the filter in response to different filter settings; the order of the filter  $M$  (i.e. the number of taps) and the number of reference channel inputs applying ANC.

## A. Creating simulated data

Throughout this paper we work with some

### A. Synthetic data

In the tests that follow, we work with representative synthetic data,  $x(t)$  generated under controlled conditions, rather than directly with the LIGO data itself. We can construct generate synthetic data for each of the constituent parts the constituents of Equation (1) - the GW signal of interest, the Gaussian noise and the noise clutter via the formulation described namely  $h(t)$ ,  $c(t)$ , and  $n(t)$ , by applying the recipe in Section II B as follows.

The GW frequency evolves in general due to the intrinsic evolution of the source. For this paper Starting with  $h(t)$  we assume that the source is isolated (i.e. it is not in a binary) and that the GW is monochromatic (i.e. all temporal derivatives of the frequency are zero signal is quasimonochromatic (i.e. the frequency varies slowly over many wave cycles if at all)). We also consider the GW source to be at a constant location with respect to the observer and neglect all contributions due to e.g. place the source at a fixed sky position and neglect for simplicity the rotation and revolution of the Earth. The latter corrections are included readily in searches with real data through the maximum likelihood  $\mathcal{F}$ -statistic [38]. Under these assumptions the GW model reduces to

$$h(t) = h \sin(2\pi\phi_{\text{GW}}(t))_0 \sin[2\pi\phi_{\text{gw}}(t)] , \quad (14)$$

where  $h$  is the constant GW amplitude and  $\phi(t)$  amplitude,  $\phi_{\text{gw}}(t)$  a random phase variable which is the integral of the underlying, piecewise linear GW frequency  $f_{\text{gw}}$  i.e.

$$\phi_{\text{GW}\text{gw}}(t) = \int_0^t ds f_{\text{gw}}(s) ds , \quad (15)$$

The GW frequency at discrete timestep  $m$  within the sampling interval  $\Delta t$  is labelled as  $f_{\text{gw}}^{(m)}$  and evolves according to and the GW frequency  $f_{\text{gw}}(t)$  evolves stochastically and piecewise linearly from one time step to the next according to

$$f_{\text{gw}}^{(m+1)}(t_{n+1}) = f_{\text{gw}}^{(m)} + \delta_m \Delta(t_{,n}) + \epsilon_n \quad (16)$$

with  $\delta_m$  a zero mean Gaussian noise at timestep  $m$  where  $\epsilon_n$  is a zero-mean Gaussian random variable, with variance  $\sigma_f^2$ , viz.

$$\delta_m \epsilon_n = \mathcal{N}(0, \Delta t \sigma_f^2) . \quad (17)$$

The Hence the synthetic GW signal  $h(t)$  is then completely described by the parameters  $h$  and  $\sigma_f^2$ , and the initial GW frequency  $h_0$ ,  $\sigma_f$ , and  $f_{\text{gw}}(t=0)$

The clutter and reference signal signals evolve according to Equations (2) and (4) respectively. For this initial study we take the reference voltage to have a constant amplitude amplitudes  $A_r(t) = a_r$ , the clutter to have a corresponding constant amplitude and  $A_c(t) = a_c$  to be constants. Similarly,  $P(t) = P = \text{constant}$ . We also assume that the modulation in the reference voltage about  $f_{\text{ac}}$  has a constant amplitude  $\Delta f_{\text{ac}}$  with a constant period  $P(t) = P$ . Throughout this work we take  $\Delta f_{\text{ac}} = 1/2\pi \text{ Hz}^{-4}$ . We define the variable  $\gamma = P^{-1}$  and explore different values for  $\gamma$ . Different values for  $P$  are explored in Section V A. Under these assumptions, Equations (2) and (4) reduce to

$$r(t) = a_r \cos \left[ 2\pi f_{\text{ac}} t + 2\pi \frac{\Delta f_{\text{ac}}}{P} \cos \left( \frac{2\pi\gamma t}{P} \right) + n_\Theta(t) \right] + n_r(t), \quad (18)$$

$$c(t) = a_c \cos [2\pi f_{\text{ac}} t' + 2\pi \cos(2\pi\gamma t') + n_\Theta(t')].$$

$$c(t) = a_c \cos \left\{ 2\pi f_{\text{ac}}(t_n - \tau_{\text{delay}}) + 2\pi \Delta f_{\text{ac}} \cos \left[ \frac{2\pi(t_n - \tau_{\text{delay}})}{P} \right] + n_\Theta(t_n - \tau_{\text{delay}}) \right\} \quad (19)$$

The synthetic reference and clutter data are then completely fully described by the amplitude parameters  $a_r, a_c$ , the central frequency  $f_{\text{ac}}$ , the timescale  $\gamma$  and the noise covariances  $\sigma_\Theta^2$ , parameters  $a_r, a_c, f_{\text{ac}}, \Delta f_{\text{ac}}, P, \sigma_\Theta^2, \sigma_r^2$ . For convenience we reparametrise  $f_{\text{ac}}$  relative to the initial GW frequency at  $t = 0$ , defining the new variable

$$\Delta f = |f_{\text{ac}} - f_{\text{gw}}(t=0)|$$

The 9 free parameters of the model

The 11 free parameters are summarised in Table ???. We have 3 ??, along with their chosen injected values. There are three amplitude parameters  $h, a_r, a_c$  for the GW, reference and clutter respectively, with  $h \ll a_c, a_r$ . There are 4 noise parameters  $\sigma_n, \sigma_\Theta, \sigma_r, \sigma_f$  for the Gaussian noise  $n(t)$ , the voltage phase noise  $n_\Theta(t)$ ,

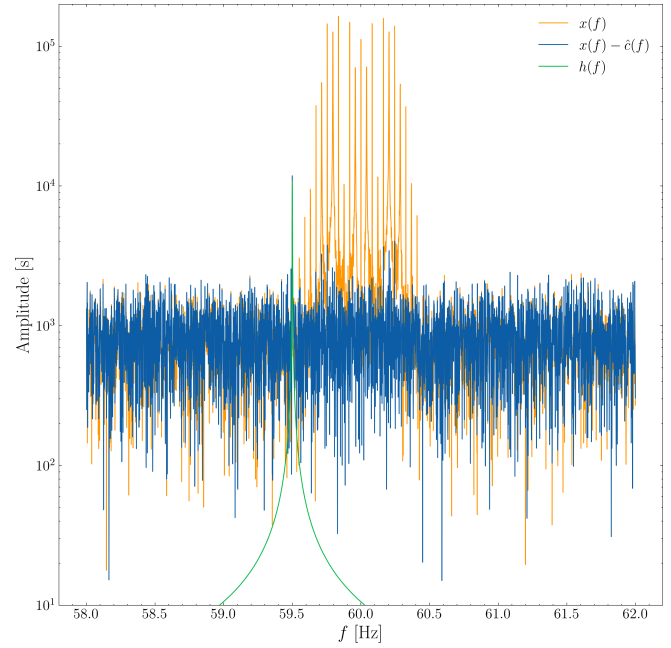


FIG. 6. Spectrum (i.e. modulus of the Fourier response transform) of the data  $x(t)$  (orange curve), the GW signal  $h(t)$  (green curve) and decluttered output of the ANC filtered data filter  $x(t) - \hat{c}(t)$  (blue curve) for a system with parameters described in Table ???. ANC filters out suppresses the excess orange spikes near 60 Hz, which corresponds to mains power that results from the interference signal about the central 60 Hz frequency by  $\approx 20$  dB.

reference signal measurement noise  $n_r(t)$  and the GW frequency noise Equation 17 respectively. Additionally we have the absolute difference between the central frequency and the initial GW frequency,  $\Delta f$  and the timescale of the modulation in the central frequency,  $\gamma$ .

Throughout this work when creating synthetic data, four noise parameters  $\sigma_n^2, \sigma_\Theta^2, \sigma_r^2$  and  $\sigma_f^2$ . In this paper  $\sigma_n^2$  and  $\sigma_r^2$  have fixed, constant values, whilst different values for  $\sigma_f^2$  and  $\sigma_\Theta^2$  are investigated in Section IV B and Section V A respectively. There are three additional parameters that specify the modulation of the central frequency:  $f_{\text{ac}}$ ,  $\Delta f_{\text{ac}}$  and  $P$ . In this paper  $f_{\text{ac}}$  is fixed at 60 Hz. The terrestrial noise parameters,  $\sigma_n^2, \sigma_r^2, \sigma_\Theta^2$  are also fixed. TK: other summary text on choice of parameters for synthetic data. Different values of  $\Delta f_{\text{ac}}$  and  $P$  are investigated in Section V A. Finally there is the initial G frequency,  $f_{\text{gw}}(t=0)$ .

## B. Representative example worked examples

In order to demonstrate the effectiveness of ANC in conjunction with an HMM Viterbi search in this section we consider To orient the reader, we start with two rep-

<sup>4</sup> TK: I have guessed that this is what is happening under the hood of the code, but Ted to verify with Sofia/Chantree with two rep-

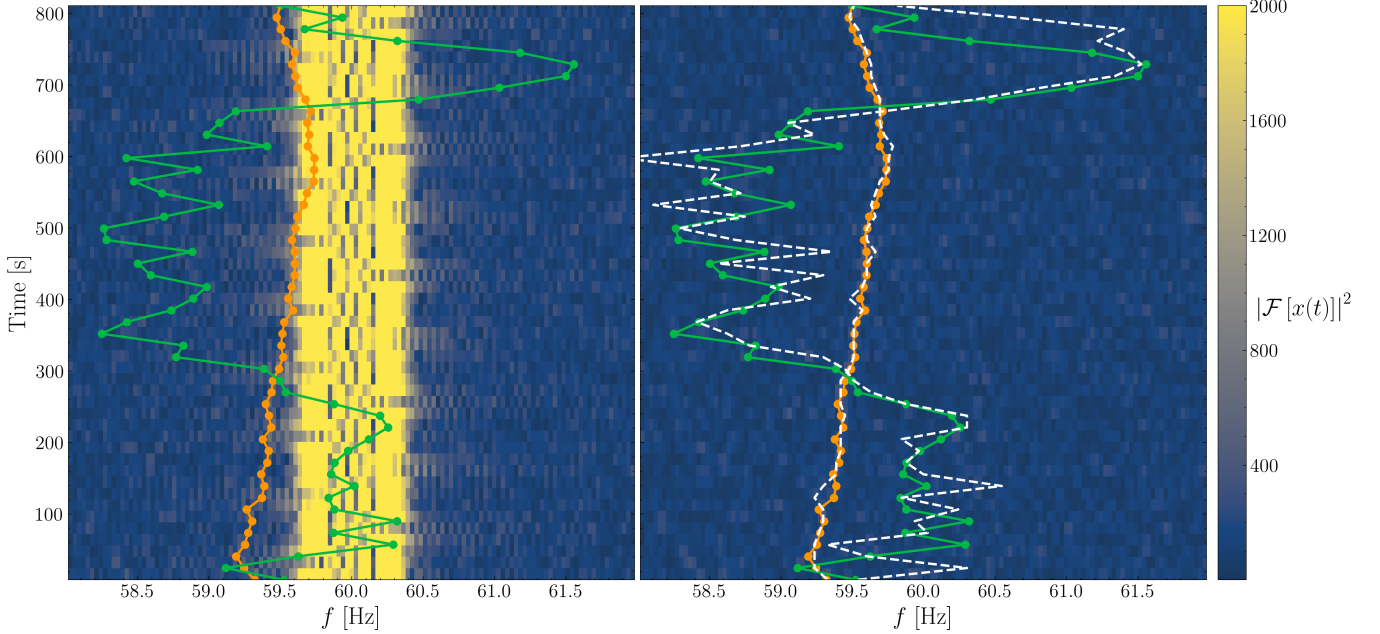


FIG. 7. Fourier amplitude spectrogram and HMM tracking of the frequency evolution of a continuous GW-CW signal with  $h = 0.025$  and  $\sigma_f^2 = \{0.01, 0.1\} \text{ Hz s}^{-1/2}$  spin wandering in the presence of 60 Hz mains power interference before (orange left panel) and green lines respectively after (right panel) using a HMM Viterbi algorithm. Left panel: before applying ANC filtering to remove the interference signal centred. Colored contours (arbitrary units; see color bar at 60Hz right) show the spectrogram of the data. Right panel: after applying ANC i.e. the squared modulus of the Fourier transform of  $x(t)$ . The Viterbi estimates of 60 Hz line is visible as a vertical yellow band in the spin wandering are noted by left panel; it cannot be discerned in the dashed coloured lines right panel. Before ANC Injected signals: lower spin wandering, the Viterbi algorithm is unable to track the with  $\sigma_f(N\Delta t)^{1/2}/f_{ac} = 0.047$  (solid orange curve), and higher spin wandering, with  $\sigma_f(N\Delta t)^{1/2}/f_{ac} = 0.15$  (solid green curve). After In both cases  $h_0/\sigma_n^2 = 0.025$ . Recovered signals: dashed white curves. Neither signal can be detected before ANC, so the Viterbi algorithm is able to track dashed white curves appear in the GW frequency accurately for both the high and low noise cases right panel only.

representative examples where  $h = 0.025$  and the stochastic GW frequency wandering is either (i) ‘low’,  $\sigma_f^2 = 0.01 \text{ Hz s}^{-1/2}$  or with  $\sigma_f(N\Delta t)^{1/2}/f_{ac} = 0.047$ , and (ii) ‘high’,  $\sigma_f^2 = 0.1 \text{ Hz s}^{-1/2}$ . All other free parameters of the model are as with  $\sigma_f(N\Delta t)^{1/2}/f_{ac} = 0.15$ . In both cases the effective SNR  $h_0/\sigma_n^2 = 0.025$ . All other parameters are specified in Table ???. At this stage we assume that we have just one single reference PEM channel. ???. For clarity of illustration, we work with a single PEM in this section and extend to multiple PEMs in Section V B

Initially we verify We start by checking visually that the ANC filter works as expected to remove removes most of the excess power from the 60Hz 60 Hz interference. In Figure 6 we show the Fourier amplitude plot the modulus of the Fourier transform of the synthetic data  $x(t)$ , the underlying GW signal  $h(t)$ , and the signal after being passed through decluttered output of the ANC filter,  $e(t) = x(t) - \hat{c}(t)$  across the frequency range 58–62 Hz, for the case where  $\sigma_f^2 = 0.01 \text{ Hz}$ , for Fourier frequencies from 58 Hz to 62 Hz for case (i). Before filtering the Fourier, the spectrum of  $x(t)$  has multiple

modes about the central 60 Hz frequency as a result of the interference clutter. This clutter obscures the power from the GW signal.  $f_{ac} = 60 \text{ Hz}$ , visible as the orange spikes in Figure 6. After filtering, this excess power is removed and the Fourier the spectrum of  $e(t)$  is flat, flatter, as indicated by the blue curve in Figure 6, with the exception of a clear feature at 59.5 Hz coincident with the central frequency of the injected GW. GW injection at  $f_{gw}(t = 0)$  (green curve). In rough terms, the ANC scheme achieves 20 dB of suppression in case (i).

Having established the ability of the ANC method scheme to filter out the interference clutter given a reference signal, we can deploy the ANC in conjunction with the Viterbi HMM. We do this by calibrating against  $r(t)$ , we pass the ANC filtered data output to the HMM and evaluate the performance of the HMM in tracking the spin-wandering continuous wave signal tracker and evaluate its performance. The results are shown in Figure 7 for the ease of both low and high frequency wandering, for a single realisation of the noise. The figure shows the Fourier amplitude spectrogram of the data spectrogram

of  $x(t)$  before and after the application of as a heat map before (left panel) and after (right panel) ANC filtering. It is clear that ANC suppresses the mains power interference, which is visible as a vertical yellow band in the left panel and is almost absent from the right panel. The spin wandering of the injected GW source (green/orange lines solid curve for higher  $\sigma_f$ , orange solid curve for lower  $\sigma_f$ ) and the Viterbi-HMM estimate (dashed orange/yellow lines) of the spin wandering is superimposed white curves for both higher and lower  $\sigma_f$ ) are superposed onto the spectrogram. In the low noise case the approximate overlap between the solid coloured and dashed white curves confirms that the ANC scheme and HMM tracker detect both injected signals successfully. For lower  $\sigma_f$ , the GW spin frequency wanders close to, but below, the 60 Hz-60 Hz interference line. In the high noise case the GW spin frequency wanders much more strongly over a larger range of frequencies and For higher  $\sigma_f$ , the GW signal crosses the interference line, presenting a more difficult challenge for the Viterbi tracking algorithm. Before ANC there is a clear feature in the Fourier spectrogram corresponding to the 60 Hz interference signal. In this case the Viterbi algorithm is unable to track the GW spin wandering frequency signal which is submerged with respect to the voltage interference at 60 Hz, which is surmounted successfully nevertheless. The time-averaged root-mean-square error in the frequency estimate is 0.038 Hz for low  $\sigma_f$  and 0.47 Hz for high  $\sigma_f$ . In contrast, neither the lower- $\sigma_f$  nor the higher- $\sigma_f$  injections are detected by the HMM tracker before ANC in the left panel.

## V. ROC CURVES

In this section, we quantify the performance of the HMM tracker, when it analyzes filtered data supplied by the ANC scheme. We do so systematically by computing receiver operating characteristic (ROC) curves as a function of key parameters of the mains power interference (Section V A) and ANC filter (Section V B). Conversely, the application of the ANC enables the interference to be removed without perturbing the gravitational wave signal. In this case the Viterbi algorithm is able to track the GW frequency wandering in both the low and high noise cases with high fidelity. Specifically, the mean squared error in the frequency estimate is  $1.4 \times 10^{-3}$  Hz for the low noise case and 0.22 Hz for the high noise case.

### A. ROC curves versus Mains power line interference parameters

With the performance of the ANC and Viterbi approach established for a single example, it is of interest to explore how the algorithm performs for different power line parameters. In this section we

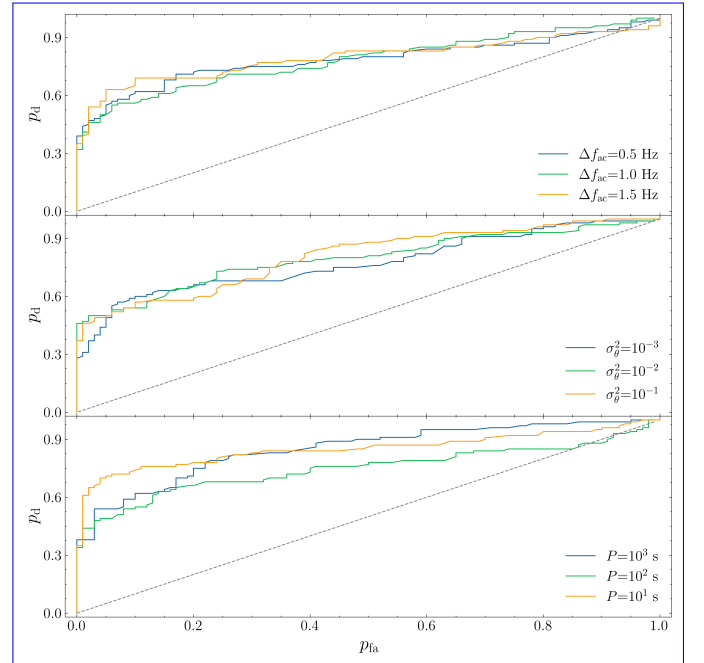


FIG. 8. Detection probability  $p_d$  as a function of false alarm probability  $p_{fa}$  (i.e. ROC curve over multiple noise realisations) for HMM tracking of a CW signal ( $h_0/c_v^2 = 0.022$ ) in conjunction with the ANC scheme, for different mains power line interference parameters. All other parameters are as specified in Table ???. There is an evident high false alarm rate for all parameters. The top panel shows different values of  $\Delta f_{ac}$ , with a low AUC value the middle panel different values of  $\sigma_\theta^2$  and the bottom panel different values of  $P$ . The high false alarm rate is a result grey dashed line in all panels denotes the performance of a random classifier. For all panels the interference not being completely removed by curves are broadly overlaid, illustrating that the HMM and ANC filterscheme is resilient to different mains power parameters. At  $p_{fa} = 0.05$  the mean  $p_d$  across the 3 curves is 0.52 (top panel), 0.48 (middle panel) and 0.58 (bottom panel). TK: we could also label as e.g.  $\Delta f_{ac}/f_{ac}$  as AM suggests. I personally find

vary  $\Delta f$  and  $\gamma$  to test how the combined ANC filter and Viterbi algorithm perform across multiple noise realisations ANC scheme and HMM tracker perform together as a function of the mains power parameters  $\Delta f_{ac}$ ,  $\sigma_\theta^2$  and  $P$ . To this end, we calculate the detection probability compared to the probability of detecting the CW signal,  $p_d$ , as a function of the false alarm probability, i.e. the receiver operating characteristic (ROC), for the Viterbi search after the data has been filtered using ANC  $p_{fa}$ , i.e. the ROC curve  $p_d(p_{fa})$ . We consider two situations three numerical experiments. In the first situation we hold  $\Delta f$  constant at  $\Delta f = 0.0$  and set  $\gamma = \{0.001, 0.01, 0.1\}$  experiment we vary  $\Delta f_{ac} = \{0.5, 1.0, 1.5\}$  Hz whilst holding constant  $\sigma_\theta^2 = 10^{-2}$  and  $P = 100$ s. In the second situation we

hold  $\gamma$  constant at  $\gamma = 0.02$  and set  $\Delta f = \{0.25, 0.5, 1.0\}$ . The results are shown in Figure 8. Whilst the underlying wandering GW frequency signal can generally be tracked well for a single noise realisation (c.f. Figure 7), we can see that for these power line parameters, across multiple noise realisations there is a high false alarm rate. This is a consequence of the interference not being completely removed and evidences how even a small quantity of clutter noise is sufficient to corrupt the search for continuous waves. To quantify the performance with a single scalar value we consider the Area Under the Curve (AUC), a common metric used to evaluate ROC curves. The AUC can be in the range  $0.5 - 1.0$ , where  $AUC = 0.5$  corresponds to the experiment we vary  $\sigma_\Theta^2 = \{10^{-3}, 10^{-2}, 10^{-1}\}$  whilst holding constant  $\Delta f_{ac} = 1.0$  Hz and  $P = 100$ s. In the third experiment we vary  $P = \{10, 10^2, 10^3\}$  s whilst holding constant  $\Delta f_{ac} = 1.0$  Hz and  $\sigma_\Theta^2 = 10^{-2}$ . For all experiments  $h_0/\sigma_v^2 = 0.022$ ,  $f_{gw}(t=0)$  is fixed to 59.9 Hz, and  $N\Delta t = 800$  s. Note that despite expecting  $\Delta f_{ac} < 0.5$ , as discussed in Section II B, in this Section we trial larger values of  $\Delta f_{ac}$  in order to provide a more difficult test for the ANC scheme and HMM tracker. All other parameters are specified in Table ??.

Figure 8 displays the ROC curves resulting from the three numerical experiments above. In the top panel the results of the first experiment are plotted, where we set  $\Delta f_{ac} = \{0.5, 1.0, 1.5\}$  Hz (blue, green and orange curves respectively). Also plotted for comparison is the performance of a random classifier (i.e. the grey dashed diagonal line in the figure) and  $AUC = 1.0$  represents a perfect classifier. For the first situation with  $\Delta f = 0.0$  and  $\gamma = \{0.001, 0.01, 0.1\}$ ,  $AUC = \{0.68, 0.65, 0.55\}$  respectively. For the second situation with  $\gamma = 0.02$  and  $\Delta f = \{0.25, 0.5, 1.0\}$ ,  $AUC = \{0.62, 0.58, 0.58\}$  respectively. Whilst the method performs better than  $(0.5, 0.5, 0.57)$  for  $\Delta f_{ac} = \{0.5, 1.0, 1.5\}$  Hz respectively. In the middle panel the results of the second experiment are plotted, where we set  $\sigma_\Theta^2 = \{10^{-3}, 10^{-2}, 10^{-1}\}$  (blue, green and orange curves respectively). Again the ANC scheme and HMM tracker outperform a random classifier for all parameters, and the results are broadly consistent across different parameter values, with  $p_d(0.05) = (0.44, 0.50, 0.49)$  for  $\sigma_\Theta^2 = \{10^{-3}, 10^{-2}, 10^{-1}\}$  respectively. In the AUC values are generally low, especially for cases where the interference has a large amplitude with a long period. In Section V B we explore the use of different parameters used for the ANC filter,

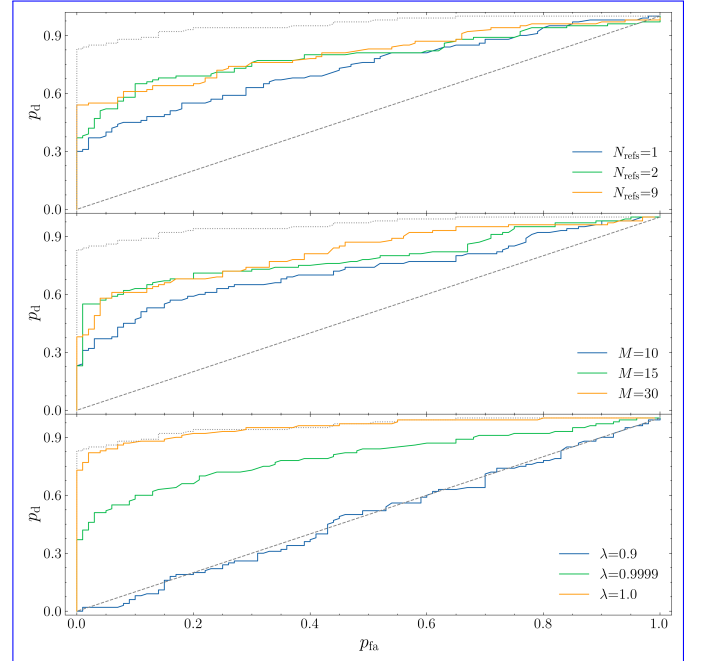


FIG. 9. ROC curve curves  $p_d(p_{fa})$  for the HMM/ANC tracking of a CW signal for different systems: System A with  $\{\gamma = 0.001, \Delta f = 0.0\}$ , System B with  $\{\gamma = 0.01, \Delta f = 0.0\}$  and System C with  $\{\gamma = 0.01, \Delta f = 0.5\}$  (dotted, dashed, solid lines respectively) ANC filter parameters. The orange lines denote top panel displays the Viterbi search run with 2 ROC curves for different number of PEM reference channels,  $N_{ref}$ , the blue lines using 1 reference channel. The green dotted line is middle panel different values of  $M$  and the detection performance in the absence bottom panel different values of ANC filtering  $\lambda$ . All panels additionally include the ROC curve for a random classifier (i.e. the lower performance limit, diagonal grey dashed line) and the ROC curve for the case where there is zero interference (i.e. the upper performance of a random classifier limit, grey dotted line). Detection using ANC filtering consistently outperforms that without ANC filtering. ANC filtering using 2 reference channels generally outperforms that using a single reference channel.

including the inclusion of additional reference channels bottom panel the results of the third experiment are plotted where we set  $P = \{10, 10^2, 10^3\}$  s (blue, green and orange curves respectively). Once again the scheme outperforms a random classifier and is robust to different parameter values, with  $p_d(0.05) = (0.7, 0.49, 0.54)$  for  $P = \{10, 10^2, 10^3\}$  s respectively.

## B. ROC curves vs. filter Filter parameters

Summary of AUC values for each of the ROC curves presented in Figure ???. Adding an extra PEM reference generally improves the detection performance, with the exception of system B. The AUC value for the zero PEM

reference case (i.e. no ANC filtering) is  $AUC = 0.55$ .

Mean square error (MSE) in the Viterbi estimates of the GW wandering spin frequency for a system with  $h = 0.025$  and  $\Delta f = 0.0$  relative to the number of taps used in the FIR filter. Up to three PEM reference channels are used. The solution for the case with zero interference clutter is also shown.

We have shown that the ANC filter used in conjunction with the Viterbi algorithm is effective at tracking the wandering GW spin frequency, but suffers from a high false alarm rate for the particular in Section V A how the ANC scheme and HMM tracker are robust to different parameters of the ANC filter that we have been using mains power interference. In this Section we investigate two section we investigate different parameters of the ANC scheme itself. Specifically, we investigate three important questions:

1. How does ANC benefit from multiple independent references?
2. What order ANC filter ( $M$ ) is required to achieve good interference cancellation?
3. How does ANC performance depend on  $\lambda$ ?

Regarding the first question, the preceding validation tests on synthetic data all assumed that we have a single PEM reference voltage measurement. However, as discussed in Section II C in practice there are multiple PEM channels measuring power line interference for LIGO (c.f. Figure ??). Specifically, in the open O3a data for O3 there are 9 PEM channels for which directly measure the mains voltage at each of the LIGO-Livingston and 7 PEM channels for LIGO-Hanford sites. Multiple PEM channels provided additional independent measurements of the reference voltage; it seems reasonable to suspect that these additional channels may aid the performance of the ANC filter. Indeed, ANC is commonly used with multiple reference signals in other electrical engineering applications such as noise cancelling headphones [55], communication intelligibility [56, 57] and cardiac monitoring [58].

In Figure ?? we present the ROC curves for 3 different example systems:

- **System A.**  $\gamma = 10^{-3}$ ,  $\Delta f = 0.0$ . Dashed lines in the figure.
- **System B.**  $\gamma = 10^{-2}$ ,  $\Delta f = 0.0$ . Dash-dotted in the figure.
- **System C.**  $\gamma = 10^{-2}$ ,  $\Delta f = 0.5$ . Solid lines in the figure.

For each system we compute the ROC curve over multiple noise realisations for both one and two reference channels (blue, and orange lines respectively). This gives us six total ROC curve solutions. For comparison we also plot the case where we run the Viterbi search for one of the example systems, but with zero PEM references (dotted

green line). The specific AUC values for each ROC curve are reported in Table ??.

We can see that for all example systems the detection probability is high with respect to the false alarm probability. The detection probability using ANC filtering is greater than without ANC filtering for all systems (i.e. the orange and blue lines are exclusively above the green dotted line). Specifically the for the zero filtering case  $AUC = 0.54$ , whilst all cases which use ANC filtering have  $AUC \geq 0.82$  and as high as  $AUC = 0.99$ . The inclusion of an additional reference channel improves the detection probability for Systems A and C, with the AUC values rising from 0.975 to 0.990 for System A and from 0.987 to 0.999 for System B. No improvement is observed for System B, with  $AUC = 0.827$  for  $N_{ref} = 1$  and  $AUC = 0.822$  for  $N_{ref} = 2$ . The lack of improvement for System B when using two PEM references suggests that for these parameters a single reference is sufficient to capture the dynamics of the interference clutter.<sup>4</sup>

Regarding the For the second question, the order of the filter, i.e. the number of taps, is a parameter that can be freely chosen in ARLS. It is important to consider the filter's robustness to the choice of  $M$ . Generally an increased number of taps is expected to improve the performance of the filter due to the increased model complexity. However, this comes at an increased computational cost and also an increased latency. For real time applications tracking the wandering of the GW frequency it is important to minimize both of these variables. In Figure ?? we plot the mean squared error (MSE) in the GW frequency estimated by Viterbi compared to the true spin-wandering frequency, averaged over multiple noise realisations. We set the system to have  $h = 0.025$  and  $\Delta f = 0.0$  and consider up-to three PEM reference channels. As a reference we also plot the error in the Viterbi estimates for the case where there is no interference clutter and so no ANC is required. We can see that generally the accuracy improves with an increased number of taps. When this work we explicitly specify the number of taps; we note that adaptive tap length methods are also available [e.g. 59–61]. Regarding the third question, the use of the forgetting factor  $\lambda$  allows ARLS to handle non-stationary systems, neglecting older data in favour of more recent data. This is useful for cases where the model parameters are time-varying, enabling more rapid convergence and effective tracking. In the case when  $\lambda = 1$ , ARLS has infinite memory and so exhibits good stability and low misadjustment. However the tracking capability can be reduced for non-stationary systems. Conversely,  $\lambda < 1$  improves the tracking at the expense of reduced stability and increased misadjustment [62]. In this paper we run ARLS using a specific value for  $\lambda$ , but note that adaptive  $\lambda$  algorithms are also available

---

<sup>4</sup> TK: Why are these results so different to Figure 8? Has the strain amplitude

[63–65].

Figure 9 displays the ROC curves for different values of the number of PEM references ( $N_{\text{ref}}$ , top panel),  $M$  is small the  $N_{\text{ref}} = 1$  solution generally outperforms the high- (middle panel) and  $\lambda$  (bottom panel). All mains power interference parameters are as specified in Table ???. Also plotted for comparison in every panel is the ROC curve of a random classifier (grey dashed diagonal line) and the ROC curve when  $c(t) = 0$  (grey dotted line). The zero interference case is included to provide a reference on the performance upper limit.

The top panel plots the ROC curves for  $N_{\text{ref}} = \{1, 2, 9\}$  (blue, green and orange curves respectively). The detection probability  $p_{\text{pd}}(0.05) = \{0.38, 0.52, 0.55\}$  for each of the respective  $N_{\text{ref}}$  solutions; in this regime the number of taps is sufficiently small to not be able to take advantage of . For comparison, in the increased information provided by the additional reference channels. Conversely as the number of taps increases , the  $N_{\text{ref}} = 3$  becomes the best performing solution. We note that rather than explicitly specifying the number of taps, adaptive tap length methods that automatically update the number of taps used are also available [e.g. 59–61]. zero interference case  $p_{\text{pd}}(0.05) = 0.85$ . It is evident that  $N_{\text{ref}} > 1$  are generally an improvement over  $N_{\text{ref}} = 1$ . However, the improvement of  $N_{\text{ref}} = 9$  over  $N_{\text{ref}} = 2$  is more modest. This suggests that the inclusion of additional reference PEM channels quickly reaches a point of diminishing returns where the interference is well-captured by a few reference channels, and adding more references beyond this point does not improve the effectiveness of the filter. The middle panel plots  $M = \{10, 15, 30\}$  (blue, green, and orange curves respectively). The detection probability  $p_{\text{pd}}(0.05) = \{0.37, 0.57, 0.58\}$  for each respective  $M$ . Analogous to the top panel, increasing  $M$  generally increases the detection probability, but the performance quickly saturates such that the ROC curves for  $M = 15$  and  $M = 30$  are highly comparable. In the bottom panel we plot  $\lambda = \{1, 2, 9\}$  (blue, green, orange curves respectively), which have respective  $p_{\text{pd}}(0.05) = \{0.38, 0.52, 0.55\}$ . A clear hierarchy is evident whereby larger values of  $\lambda$  increase the detection probability. For the synthetic data in this paper  $\lambda = 1$  is advantageous for detection since the interference is quasi-stationary (c.f. Equation 19). Consequently, discounting older data with  $\lambda < 1$  inhibits the ability of the ANC scheme to filter out the interference. We defer investigation of non-stationary interference (c.f. Equation 4) to a future work. For application to real astrophysical data  $\lambda$  will need to be selected optimally e.g. [66].

## VI. CONCLUSIONS

In this paper we demonstrate a new line subtraction method based on adaptive noise cancellation for use in continuous gravitational wave searches. We use an adaptive recursive least squares method in conjunction with an independent, known PEM reference signal to suppress the interference from a long-lived narrow spectral feature. We then search for the continuous wave signal using a HMM Viterbi algorithm. We test our method on synthetic data containing the 60 Hz spectral interference line due to the North American power grid. We show how the the ANC and Viterbi algorithm together are able to successfully track the spin-wandering continuous GW signal near the 60 Hz line. We test the method over multiple noise realisations and show TK: to confirm. The performance of the filter is generally improved with an increased number of reference signals and at an increased model orderThe method is shown to be robust to different mains power interference parameters, whilst larger values of  $N_{\text{ref}}$ ,  $M$  and  $\lambda$  generally increase the effectiveness of the ANC filter and the probability of detecting the GW signal.

- 
- [1] L. Blackburn, L. Cadonati, S. Caride, S. Caudill, S. Chatterji, N. Christensen, J. Dalrymple, S. Desai, A. Di Credico, G. Ely, *et al.*, *Classical and Quantum Gravity* **25**, 184004 (2008), arXiv:0804.0800 [gr-qc].
- [2] J. Aasi, J. Abadie, B. P. Abbott, R. Abbott, T. D. Abbott, M. Abernathy, T. Accadia, F. Acernese, C. Adams, *et al.*, *Classical and Quantum Gravity* **29**, 155002 (2012), arXiv:1203.5613 [gr-qc].
- [3] J. Aasi, J. Abadie, B. P. Abbott, R. Abbott, T. Abbott, M. R. Abernathy, T. Accadia, F. Acernese, C. Adams, T. Adams, *et al.*, *Classical and Quantum Gravity* **32**, 115012 (2015), arXiv:1410.7764 [gr-qc].
- [4] B. P. Abbott, R. Abbott, T. D. Abbott, M. R. Abernathy, F. Acernese, K. Ackley, M. Adamo, C. Adams, T. Adams, P. Addesso, *et al.*, *Classical and Quantum Gravity* **33**, 134001 (2016), arXiv:1602.03844 [gr-qc].
- [5] J. Glanzer, S. Soni, J. Spoon, A. Effler, and G. González, arXiv e-prints , arXiv:2304.07477 (2023), arXiv:2304.07477 [astro-ph.IM].
- [6] LIGO Scientific Collaboration, J. Aasi, B. P. Abbott, R. Abbott, T. Abbott, M. R. Abernathy, K. Ackley, C. Adams, T. Adams, P. Addesso, and et al., *Classical and Quantum Gravity* **32**, 074001 (2015), arXiv:1411.4547 [gr-qc].
- [7] B. P. Abbott, R. Abbott, T. D. Abbott, S. Abraham, F. Acernese, K. Ackley, C. Adams, V. B. Adya, C. Affeldt, M. Agathos, *et al.*, *Classical and Quantum Gravity* **37**, 055002 (2020), arXiv:1908.11170 [gr-qc].
- [8] .
- [9] T. Akutsu, M. Ando, K. Arai, Y. Arai, S. Araki, A. Araya, N. Aritomi, H. Asada, Y. Aso, S. Bae, *et al.*, *Progress of Theoretical and Experimental Physics* **2021**, 05A102 (2021), arXiv:2009.09305 [gr-qc].
- [10] P. Nguyen, R. M. S. Schofield, A. Effler, C. Austin, V. Adya, M. Ball, S. Banagiri, K. Banowetz, C. Billman, C. D. Blair, *et al.*, *Classical and Quantum Gravity* **38**, 145001 (2021), arXiv:2101.09935 [astro-ph.IM].
- [11] P. B. Covas, A. Effler, E. Goetz, P. M. Meyers, A. Neunzert, M. Oliver, B. L. Pearlstone, V. J. Roma, R. M. S. Schofield, V. B. Adya, and et al., *Phys. Rev. D* **97**, 082002 (2018), arXiv:1801.07204 [astro-ph.IM].
- [12] O. J. Piccinni, *Galaxies* **10**, 72 (2022), arXiv:2202.01088 [gr-qc].
- [13] K. Riles, *Living Reviews in Relativity* **26**, 3 (2023), arXiv:2206.06447 [astro-ph.HE].
- [14] K. Wette, *Astroparticle Physics* **153**, 102880 (2023), arXiv:2305.07106 [gr-qc].
- [15] R. Abbott, H. Abe, F. Acernese, K. Ackley, N. Adhikari, R. X. Adhikari, V. K. Adkins, V. B. Adya, C. Affeldt, D. Agarwal, M. Agathos, K. Agatsuma, N. Aggarwal, O. D. Aguiar, *et al.* (LIGO Scientific Collaboration, Virgo Collaboration, and KAGRA Collaboration), *Phys. Rev. D* **106**, 062002 (2022).
- [16] R. Abbott, T. D. Abbott, S. Abraham, F. Acernese, K. Ackley, A. Adams, C. Adams, R. X. Adhikari, V. B. Adya, C. Affeldt, D. Agarwal, M. Agathos, K. Agatsuma, N. Aggarwal, O. D. Aguiar, *et al.*, *Astrophys. J.* **921**, 80 (2021), arXiv:2105.11641 [astro-ph.HE].
- [17] R. Abbott, T. D. Abbott, F. Acernese, K. Ackley, C. Adams, N. Adhikari, R. X. Adhikari, V. B. Adya, C. Affeldt, D. Agarwal, M. Agathos, K. Agatsuma, N. Aggarwal, O. D. Aguiar, L. Aiello, *et al.*, *Astrophys. J.* **932**, 133 (2022), arXiv:2112.10990 [gr-qc].
- [18] D. Davis, J. S. Areeda, B. K. Berger, R. Bruntz, A. Effler, R. C. Essick, R. P. Fisher, P. Godwin, E. Goetz, A. F. Helmling-Cornell, *et al.*, *Classical and Quantum Gravity* **38**, 135014 (2021), arXiv:2101.11673 [astro-ph.IM].
- [19] D. Davis and M. Walker, *Galaxies* **10** (2022), 10.3390/galaxies10010012.
- [20] B. P. Abbott, R. Abbott, T. D. Abbott, M. R. Abernathy, F. Acernese, K. Ackley, C. Adams, T. Adams, P. Addesso, R. X. Adhikari, *et al.*, *Classical and Quantum Gravity* **35**, 065010 (2018), arXiv:1710.02185 [gr-qc].
- [21] J. Lee, S. H. Oh, K. Kim, G. Cho, J. J. Oh, E. J. Son, and H. M. Lee, *Phys. Rev. D* **103**, 123023 (2021).
- [22] B. Steltner, M. A. Papa, and H.-B. Eggenstein, *Phys. Rev. D* **105**, 022005 (2022), arXiv:2105.09933 [gr-qc].
- [23] J. C. Driggers, M. Evans, K. Pepper, and R. Adhikari, *Review of Scientific Instruments* **83**, 024501 (2012), arXiv:1112.2224 [gr-qc].
- [24] V. Tiwari, M. Drago, V. Frolov, S. Klimenko, G. Mitselmakher, V. Nécula, G. Prodi, V. Re, F. Salemi, G. Vevodato, and I. Yakushin, *Classical and Quantum Gravity* **32**, 165014 (2015), arXiv:1503.07476 [gr-qc].
- [25] D. Davis, T. Massinger, A. Lundgren, J. C. Driggers, A. L. Urban, and L. Nuttall, *Classical and Quantum Gravity* **36**, 055011 (2019), arXiv:1809.05348 [astro-ph.IM].
- [26] J. C. Driggers, S. Vitale, A. P. Lundgren, M. Evans, K. Kawabe, S. E. Dwyer, K. Izumi, R. M. S. Schofield, A. Effler, D. Sigg, P. Fritschel, M. Drago, *et al.*, *Phys. Rev. D* **99**, 042001 (2019), arXiv:1806.00532 [astro-ph.IM].
- [27] P. Jung, S. H. Oh, Y.-M. Kim, E. J. Son, T. Yokozawa, T. Washimi, and J. J. Oh, *Phys. Rev. D* **106**, 042010 (2022).
- [28] A. Marin, D. Shoemaker, and R. Weiss, “Subtracting narrow-band noise from ligo strain data in the third observing run,” LIGO Technical Report LIGO-T970127-02-D.
- [29] E. Cuoco, J. Powell, M. Cavaglià, K. Ackley, M. Bejger, C. Chatterjee, M. Coughlin, S. Coughlin, P. Easter, R. Essick, H. Gabbard, T. Gebhard, S. Ghosh, L. Haegel, A. Iess, D. Keitel, Z. Marka, S. Marka, F. Morawski, T. Nguyen, R. Ormiston, M. Puerrer, M. Razzano, K. Staats, G. Vajente, and D. Williams, arXiv e-prints , arXiv:2005.03745 (2020), arXiv:2005.03745 [astro-ph.HE].
- [30] G. Vajente, Y. Huang, M. Isi, J. C. Driggers, J. S. Kissel, M. J. Szczepańczyk, and S. Vitale, *Phys. Rev. D* **101**, 042003 (2020), arXiv:1911.09083 [gr-qc].
- [31] R. Ormiston, T. Nguyen, M. Coughlin, R. X. Adhikari, and E. Katsavounidis, arXiv e-prints , arXiv:2005.06534 (2020), arXiv:2005.06534 [astro-ph.IM].
- [32] T. S. Yamamoto, S. Kuroyanagi, and G.-C. Liu, *Phys. Rev. D* **107**, 044032 (2023).
- [33] S. J. Zhu, M. A. Papa, and S. Walsh, *Phys. Rev. D* **96**, 124007 (2017), arXiv:1707.05268 [gr-qc].
- [34] D. Jones, L. Sun, J. Carlin, L. Dunn, M. Millhouse, H. Middleton, P. Meyers, P. Clearwater, D. Beniwal, L. Strang, A. Vargas, and A. Melatos, *Phys. Rev. D* **106**, 123011 (2022).

- [35] S. Suvorova, L. Sun, A. Melatos, W. Moran, and R. J. Evans, *Phys. Rev. D* **93**, 123009 (2016), arXiv:1606.02412 [astro-ph.IM].
- [36] The LIGO Scientific Collaboration, the Virgo Collaboration, the KAGRA Collaboration, R. Abbott, T. D. Abbott, F. Acernese, K. Ackley, C. Adams, N. Adhikari, R. X. Adhikari, *et al.*, arXiv e-prints , arXiv:2111.03606 (2021), arXiv:2111.03606 [gr-qc].
- [37] “Gravitational Wave Open Science Center,” <https://www.gwopenscience.org/>.
- [38] P. Jaranowski, A. Królak, and B. F. Schutz, *Phys. Rev. D* **58**, 063001 (1998), arXiv:gr-qc/9804014 [gr-qc].
- [39] D. M. Macleod, J. S. Areeda, S. B. Coughlin, T. J. Massinger, and A. L. Urban, *SoftwareX* **13**, 100657 (2021).
- [40] P. Welch, *IEEE Transactions on Audio and Electroacoustics* **15**, 70 (1967).
- [41] B. Widrow, J. Glover, J. McCool, J. Kaunitz, C. Williams, R. Hearn, J. Zeidler, J. Eugene Dong, and R. Goodlin, *Proceedings of the IEEE* **63**, 1692 (1975).
- [42] S. Haykin, *Adaptive Filter Theory*, 4th ed. (Prentice Hall, Upper Saddle River, New Jersey, 07458, 2002).
- [43] M. H. Hayes, *Statistical Digital Signal Processing and Modeling*, 1st ed. (John Wiley & Sons, Inc., USA, 1996).
- [44] E. C. Ifeachor and B. W. Jervis, *Digital Signal Processing: A Practical Approach*, 2nd ed. (Pearson Education, 2002).
- [45] L. Ljung, *System Identification: Theory for the User*, Prentice Hall information and system sciences series (Prentice Hall PTR, 1999).
- [46] T. Söderström and P. Stoica, *System Identification*, Prentice-Hall Software Series (Prentice Hall, 1989).
- [47] A. Viterbi, *IEEE Transactions on Information Theory* **13**, 260 (1967).
- [48] B. G. Quinn and E. J. Hannan, *The Estimation and Tracking of Frequency*, Cambridge Series in Statistical and Probabilistic Mathematics (Cambridge University Press, 2001).
- [49] L. S. Collaboration and V. Collaboration (LIGO Scientific Collaboration and Virgo Collaboration), *Phys. Rev. D* **95**, 122003 (2017).
- [50] L. S. Collaboration and V. Collaboration (LIGO Scientific Collaboration and Virgo Collaboration), *Phys. Rev. D* **100**, 122002 (2019).
- [51] M. Isi, L. Sun, R. Brito, and A. Melatos, *Phys. Rev. D* **99**, 084042 (2019).
- [52] L. Sun, A. Melatos, S. Suvorova, W. Moran, and R. J. Evans, *Phys. Rev. D* **97**, 043013 (2018), arXiv:1710.00460 [astro-ph.IM].
- [53] V. C. LIGO Scientific Collaboration and K. Collaboration (LIGO Scientific Collaboration, Virgo Collaboration, and KAGRA Collaboration), *Phys. Rev. D* **106**, 062002 (2022).
- [54] A. F. Vargas and A. Melatos, *Phys. Rev. D* **107**, 064062 (2023), arXiv:2208.03932 [gr-qc].
- [55] J. Cheer, V. Patel, and S. Fontana, *The Journal of the Acoustical Society of America* **145**, 3095 (2019), [https://pubs.aip.org/asa/jasa/article-pdf/145/5/3095/15336560/3095\\_1\\_online.pdf](https://pubs.aip.org/asa/jasa/article-pdf/145/5/3095/15336560/3095_1_online.pdf).
- [56] S. M. Kuo and J. Kunduru, *Journal of the Franklin Institute* **333**, 669 (1996).
- [57] K. Kokkinakis, B. Azimi, Y. Hu, and D. R. Friedland, *Trends in Amplification* **16**, 102 (2012), pMID: 22923425, <https://doi.org/10.1177/1084713812456906>.
- [58] S. S. Chowdhury, R. Hyder, M. S. B. Hafiz, and M. A. Haque, *IEEE Journal of Biomedical and Health Informatics* **22**, 450 (2018).
- [59] Y. Gong and C. Cowan, in *2004 IEEE International Conference on Acoustics, Speech, and Signal Processing*, Vol. 2 (2004) pp. ii–825.
- [60] A. Kar and M. Swamy, *Signal Processing* **131**, 422 (2017).
- [61] A. Kar, A. Anand, and M. Swamy, *Applied Acoustics* **158**, 107043 (2020).
- [62] S. Ciocchina, C. Paleologu, J. Benesty, and A. A. Enescu, in *2009 International Symposium on Signals, Circuits and Systems* (2009) pp. 1–4.
- [63] M. Mahadi, T. Ballal, M. Moinuddin, and U. M. Al-Saggaf, *Applied Sciences* **12** (2022), 10.3390/app12042077.
- [64] S.-H. Leung and C. So, *IEEE Transactions on Signal Processing* **53**, 3141 (2005).
- [65] C. Paleologu, J. Benesty, and S. Ciocchina, *IEEE Signal Processing Letters* **15**, 597 (2008).
- [66] S. Van Vaerenbergh, I. Santamaría, and M. Lázaro-Gredilla, in *2012 IEEE International Workshop on Machine Learning for Signal Processing* (2012) pp. 1–6.

## ACKNOWLEDGMENTS

This research has made use of data, software and/or web tools obtained from the Gravitational Wave Open Science Center (<https://www.gwopenscience.org/>), a service of LIGO Laboratory, the LIGO Scientific Collaboration and the Virgo Collaboration. LIGO is funded by the U.S. National Science Foundation. Virgo is funded by the French Centre National de Recherche Scientifique (CNRS), the Italian Istituto Nazionale della Fisica Nucleare (INFN) and the Dutch Nikhef, with contributions by Polish and Hungarian institutes. This research was supported by the Australian Research Council Centre of Excellence for Gravitational Wave Discovery (OzGrav), grant number CE170100004.